Supporting information

Internal strain-driven bond manipulation and band engineering in $Bi_{2-x}Sb_xYO_4Cl$ photocatalysts with triple fluorite layers

Artem Gabov,[a, b] Daichi Kato,[a*] Hiroki Ubukata,[a] Ryotaro Aso,[c] Naoji Kakudou,[a] Koji Fujita,[d] Hajime Suzuki,[a] Osamu Tomita,[a] Akinori Saeki,[e] Ryu Abe,[a] Smagul Zh Karazhanov,[f*] and Hiroshi Kageyama[a*]

[a]Department of Energy and Hydrocarbon Chemistry, Graduate School of Engineering, Kyoto University, Nishikyo-ku, Kyoto 615-8510, Japan

[b]National Research Nuclear University MEPhI (Moscow Engineering Physics Institute), 31 Kashirskoye Shosse, Moscow 115409, Russia

[c]Department of Applied Quantum Physics and Nuclear Engineering, Kyushu University, Fukuoka 819-0395, Japan

[d]Department of Material Chemistry, Graduate School of Engineering, Kyoto University, Kyoto 615-8510, Japan

[e]Department of Applied Chemistry, Graduate School of Engineering, Osaka University, Osaka 565-0871, Japan

[f]Department for Solar Energy Materials and Technologies, Institute for Energy Technology, NO 2027, Kjeller, Norway

Table of Contents

1. Details of Rietveld refinement and calculations of bond length and BVS

For $0 \le x \le 1.25$, Rietveld refinements were performed assuming the Bi_2YO_4Cl model with Bi/Sb at the 2*h* site, Y at the 1*a* site, O at the 4*i* site, and Cl at the 1*b* site.[1] For $1.5 \le x \le 2$, we used the Sb_2YO_4Cl model with Bi/Sb at the 8*g* site, Y at the 2*a* and 2*c* sites, O at the 8*g* site, and Cl at the 2*b* and 2*c* sites.[2] For the Sb_2YO_4Cl model ($1.5 \le x \le 2$), isotropic atomic displacement parameters (U_{iso}) of cations and anions were refined separately because otherwise U_{iso} of O becomes negative, due to the low sensitivity of X-ray diffraction to the position of light oxygen atoms in the presence of much heavier elements such as Bi. In both models, Bi and Sb were placed at the single crystallographic site assuming their random distribution, and their U_{iso} values were restricted to be equal. Refined atomic positions and parameters are listed in Table S2. This data was used to calculate the lengths of *A*–O, *A*–Cl, and Y–O bonds. For the Sb_2YO_4Cl structure ($1.5 \le x \le 2$), which has two Y and O sites, the average lengths of bonds were considered. Note that we averaged the values from the four nearest oxygens for the (Bi,Sb)–O length in all the compositions including the $1.5 \le x \le 2$ phases with the Sb_2YO_4Cl structure. The change in bond length (Fig. 6a) was shown relative to that of Bi_2YO_4Cl. The same data, obtained by Rietveld refinement, was used for the calculation of BVS (Fig. 6b, c). In the case of the Sb_2YO_4Cl structure ($1.5 \le x \le 2$) with two Y and O sites, the BVS are averaged over the sites. The global instability index (GII) was also calculated in the same manner (Fig. 6d).

2. Details of the discussion about strain effect and bond breaking

First, it is important to distinguish whether there is no bond or if the bond is just elongated. In the case of Bi_2MO_4Cl (*M* = Bi, La) and Sb_2YO_4Cl, the presence of bond breaking is evident because the corresponding Bi–O and Sb–O distances (3.32 Å, 3.71 Å, and 3.00 Å, respectively) are well beyond the sum of the ionic radii (Table S5). Moreover, the bond valence of the cleaved Bi/Sb–O is negligibly small compared to that from the bonding oxygen (Table S5). Specifically, Bi/Sb–O bonds with negligible bond valence (< 0.1) are not shown in this paper.

While we discuss the role and impact of biaxial strain based on the change of bond length and BVS in the main text, they can also be found in the change of volume of YO_8 and AO_4 (*A* = Bi/Sb) polyhedra. In the range of $0 \le x \le 0.5$, the volume of both YO_8 and AO_4 polyhedra remains almost constant (Fig. S5). Further Sb substitution ($0.5 \le x \le 1.25$) leads to a sharp increase in AO_4 volume while that of YO_8 remains almost constant, supporting the flexible nature of the *A*–O sublayer and rigid nature of the Y–O sublayer. Y becomes slightly underbonded but maintains almost ideal coordination after the phase transition, involving the rotation and slight expansion of YO_8 polyhedra (Fig. S5).

It is rather surprising that the phase transition does not occur until $x = 1.5$. This is probably because, as shown in Fig. 6b, Bi in the distorted Sb_2YO_4Cl-type structure is highly overbonded and thus the Bi concentration, $(2–x)/2 \times 100$, needs to be decreased to less than 25%. In addition, the presence of the Cl layer forming heteroleptic coordination to the *A*-site (Bi/Sb) may help in suppressing the phase transition,[3] since a slight decrease in the (Bi,Sb)–Cl distance could partially compensate for the (Bi,Sb)–O underbonding. It is worth mentioning that lattice instability induced by bond breaking, characterized by phonon softening, can often lead to intriguing phenomena around the phase boundary, such as the emergence of ferromagnetism in $SrCo_2(Ge_{1-x}P_x)_2$[4] and superconductivity in $Au_{1-x}Pt_xTe_2$.[5] Thus, the anomalous elongation of the Sb–O bond length is likely caused by significant lattice instability induced by competition with bond breaking.

The concept of "strain" can be applied to general layered materials. For $Bi_{12}O_{17}Cl_2$ with a sextuple fluorite-like layer, the corrugation of the fluorite layer and its removal by $O^{2-}/2F^-$ exchange suggest intrinsic strain in compounds with thicker fluorite layers.[6] The mechanism of phase transition suggested for Sb substitution can also rationalize the bond breaking in Bi_2LaO_4Cl and Bi_3O_4Cl structures with a triple fluorite layer as described in the main text.[7] Apart from oxyhalides, the bond breaking due to the biaxial strain effect from adjacent layers was previously addressed in the high-pressure synthesis of $Ba_2ZnO_2Ag_2Te_{2.5}$.[8] This compound exhibits elongated Zn–O bonds due to the increased size mismatch with the soft Ag_2Te_2 layer upon depressurization.

3. Details of PDF analysis

The stereochemical activity of lone pair cations can often cause local structural distortion, such as their off-centring or reorientation. Therefore, we considered that the change in stereochemical activity of the Sb lone pair state could possibly affect the local structure, though in $Bi_{2-x}Sb_xYO_4Cl$ the average structure is preserved in the range of $0 < x < 1.5$. To examine this, we performed pair distribution function (PDF) analysis. The maximum momentum transfer value of the SPXRD data for the PDF analysis was $Q = 18.87$ Å^{-1}. The PDFgetX3 program[9] and PDFfit2 software[10] were used for Fourier transformation and further refinement, respectively. Figure S6 shows the profiles of X-ray PDF data for compositions with $x = 0$, 0.5, and 1 assuming the structure obtained by Rietveld refinements, which provide good fits in the range of shorter regions ($2 < r < 12$ Å) as well as in wider regions (Table S3). In addition, we did not observe any systematic change in atomic displacement parameters. These observations indicate the absence of significant deviation between the local and average structures and the absence of systematic change in the local structure with increasing Sb ratio (Table S3). It should be noted that the fit becomes slightly worse for larger *x* compositions. This is probably because the increase in Sb ratio leads to a decrease in the

intensity of PDF data due to the large X-ray absorption of Sb decreasing the resolution at higher angles (i.e., higher Q) region of the collected SPXRD data.

4. Supporting figures

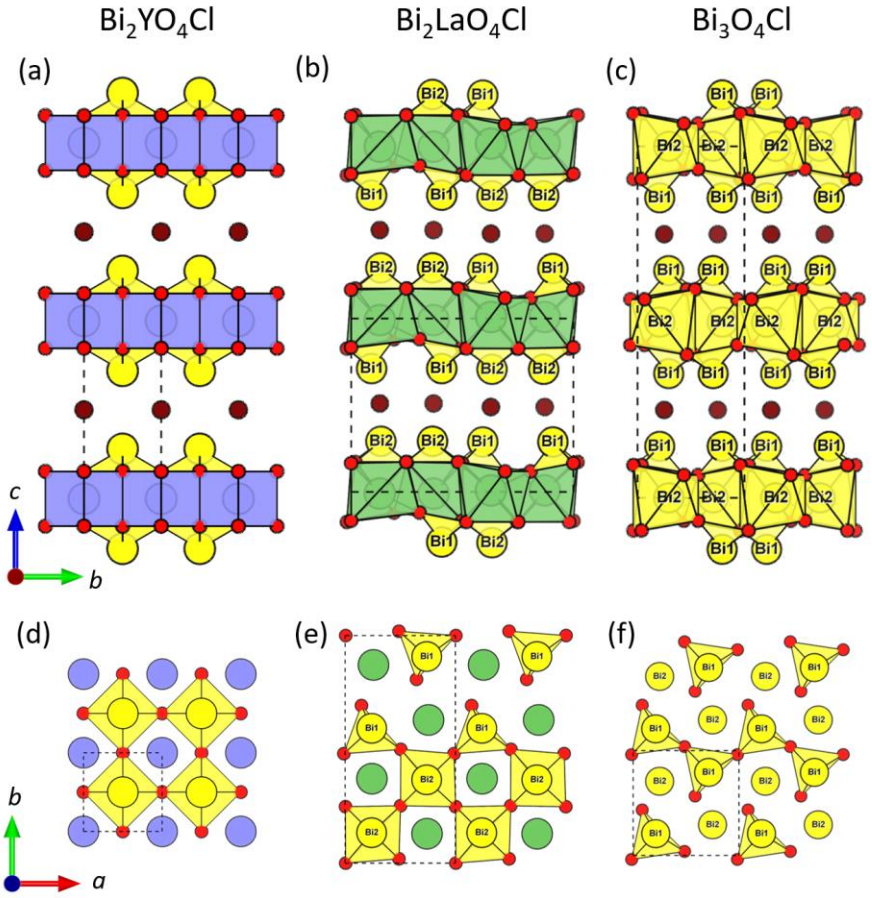

Figure S1. Comparison of (a, d) Bi_2YO_4Cl, (b, e) Bi_2LaO_4Cl and (c, f) Bi_3O_4Cl structure. The latter two feature triple fluorite layers with a *n*-zigzag arrangement (n = 2 for Bi_2LaO_4Cl and n = 1 for Bi_2BiO_4Cl),[7] while Bi_2YO_4Cl features an undistorted fluorite layer. Bi/Sb–O bonds with negligible bond valence (< 0.1) are not drawn (Table S5).

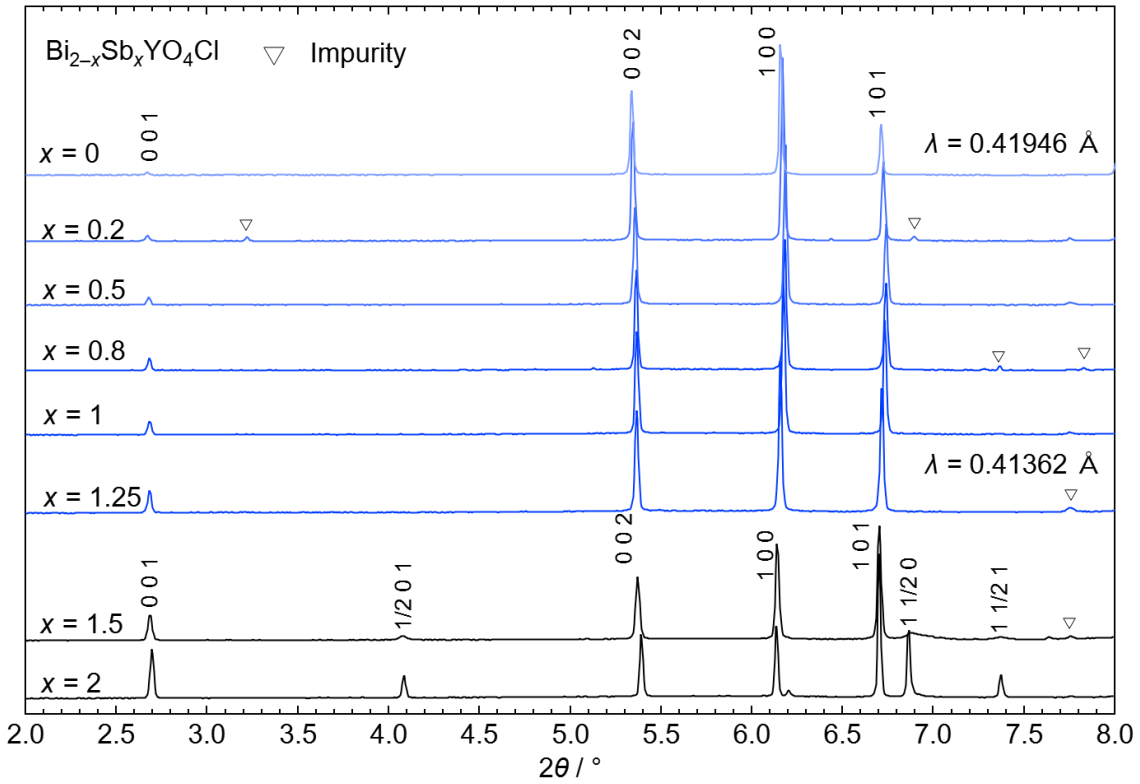

Figure S2. Enlarged SPXRD patterns of $Bi_{2-x}Sb_xYO_4Cl$ ($0 \leq x \leq 2$). The samples with $x \leq 1.25$ are indexed with the *P*4/*mmm* space group (Bi_2YO_4Cl structure). Superstructure peaks such as (1/2 0 1) can be observed for $x \geq 1.5$.

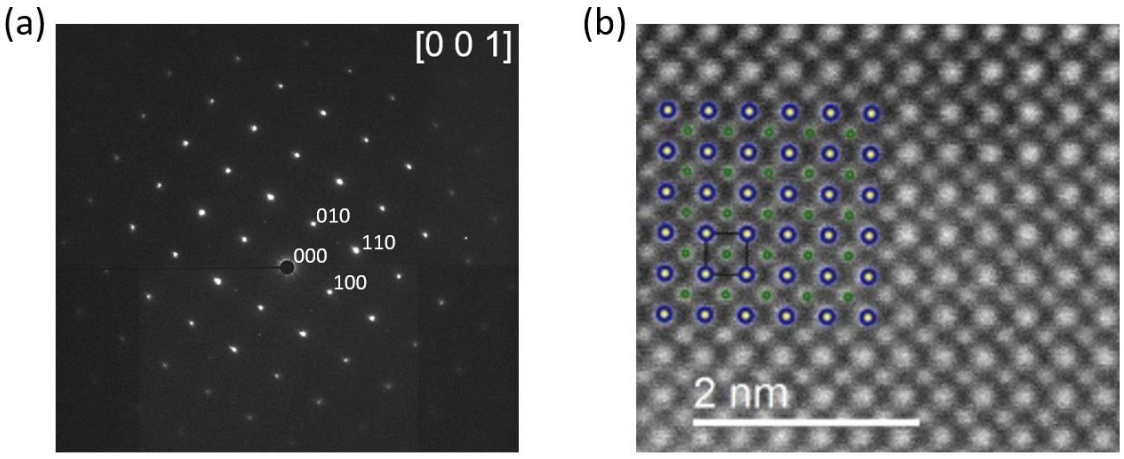

Figure S3. (a) Selected area electron diffraction (SAED) pattern along the [001] direction and (b) a high-angle annular dark-field scanning transmission electron microscopy (HAADF-STEM) image of $BiSbYO_4Cl$ (x = 1). Green, blue, and yellow balls correspond to Sb/Bi, Y, and Cl atoms, respectively. Additional spots seen on the SAED pattern cannot be systematically indexed, and hence they are likely to originate from tiny impurities or from another crystalline particle with different orientations.

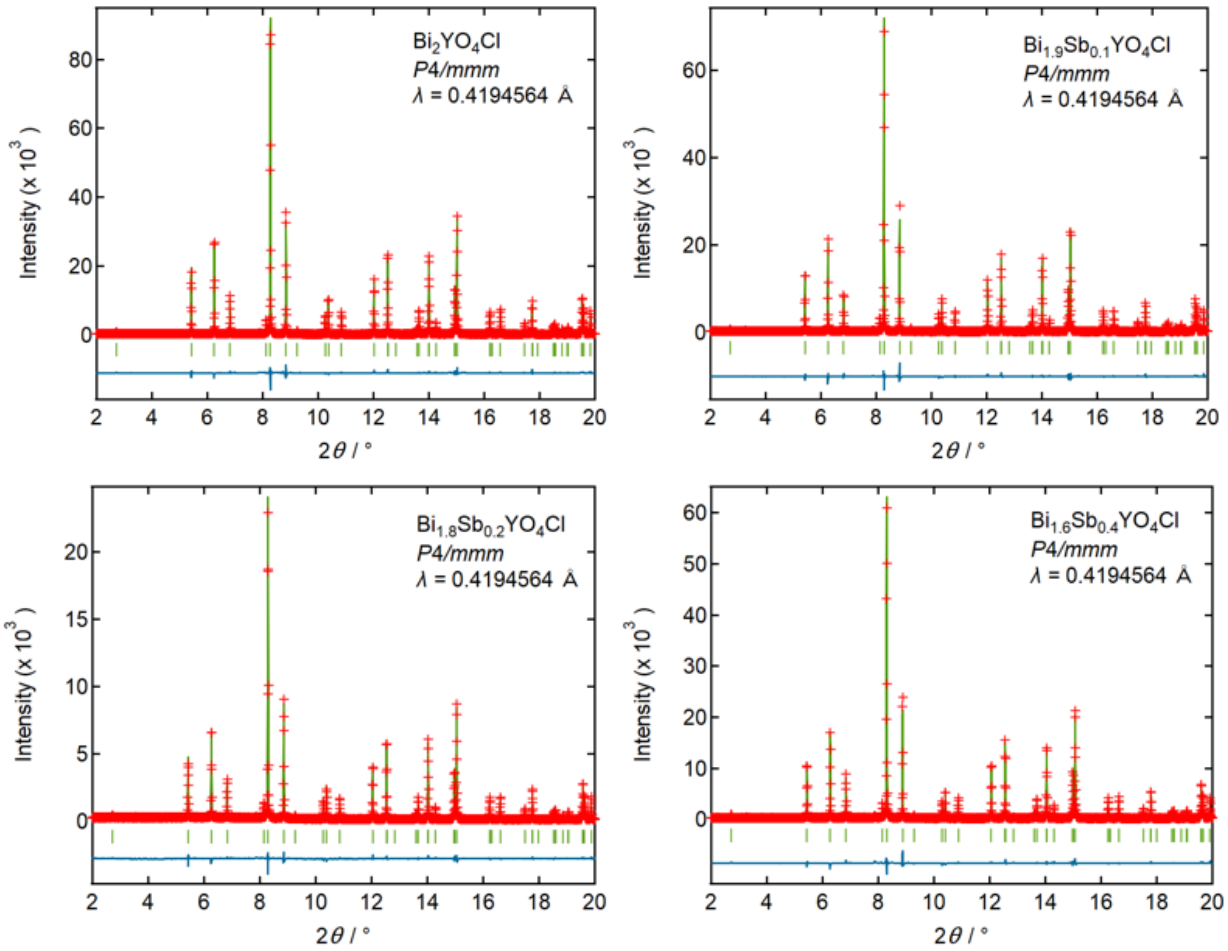
Bi2YO4Cl
P4/mmm
λ = 0.4194564 Å
Bi1.9Sb0.1YO4Cl
P4/mmm
λ = 0.4194564 Å
Bi1.8Sb0.2YO4Cl
P4/mmm
λ = 0.4194564 Å
Bi1.6Sb0.4YO4Cl
P4/mmm
λ = 0.4194564 Å
Intensity (x 10^3)
2θ / °

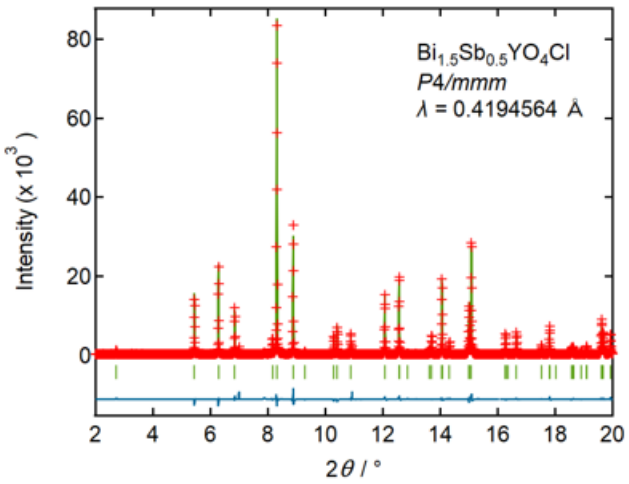
Bi1.5Sb0.5YO4Cl
P4/mmm
λ = 0.4194564 Å
Intensity (x 10^3)
2θ / °

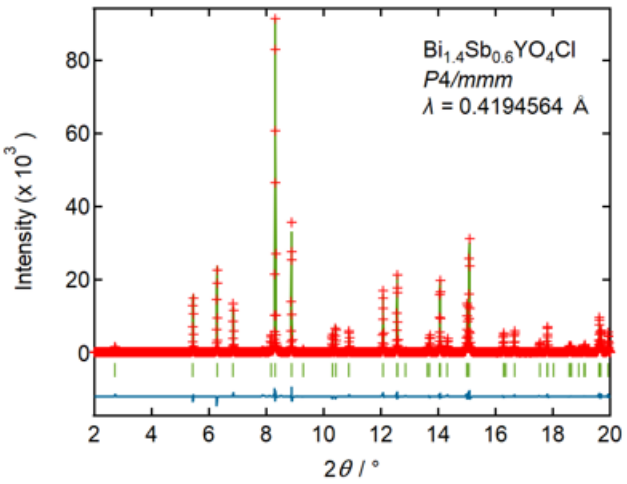
Bi1.4Sb0.6YO4Cl
P4/mmm
λ = 0.4194564 Å
Intensity (x 10^3)
2θ / °

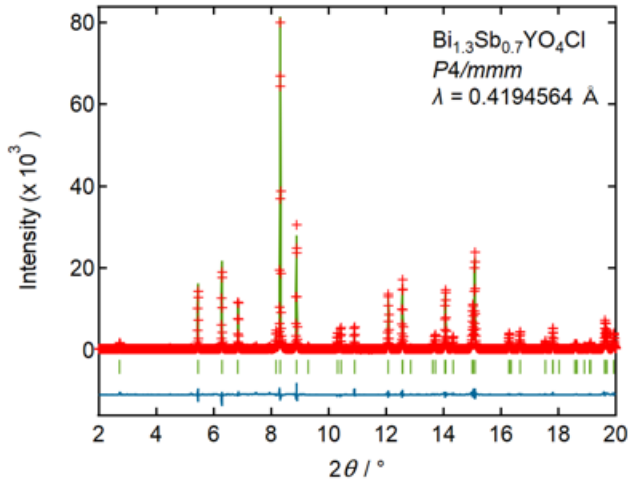
Bi1.3Sb0.7YO4Cl
P4/mmm
λ = 0.4194564 Å
Intensity (x 10^3)
2θ / °

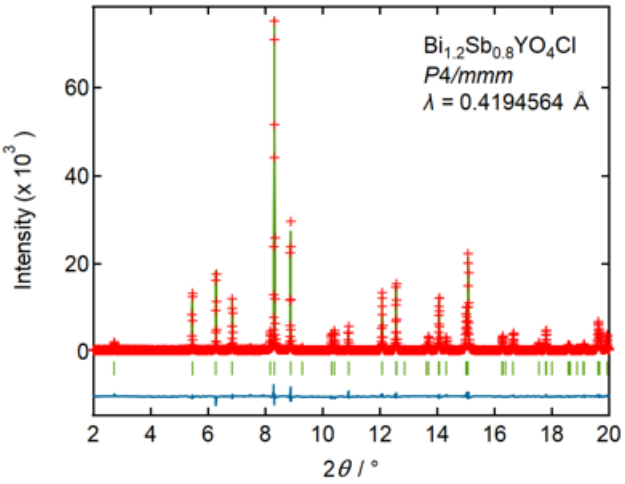
Bi1.2Sb0.8YO4Cl
P4/mmm
λ = 0.4194564 Å
Intensity (x 10^3)
2θ / °

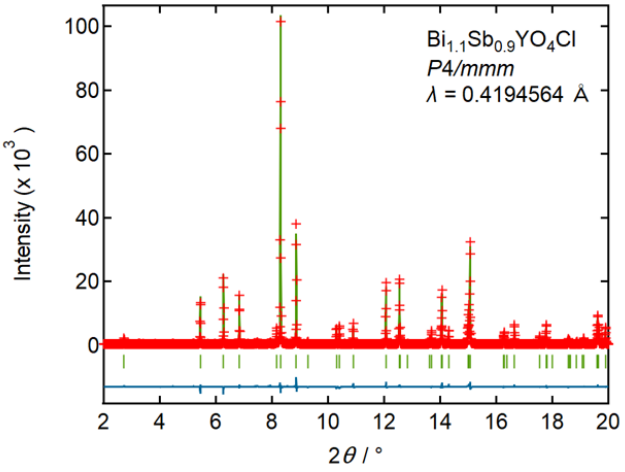
Bi1.1Sb0.9YO4Cl
P4/mmm
λ = 0.4194564 Å
Intensity (x 10^3)
2θ / °

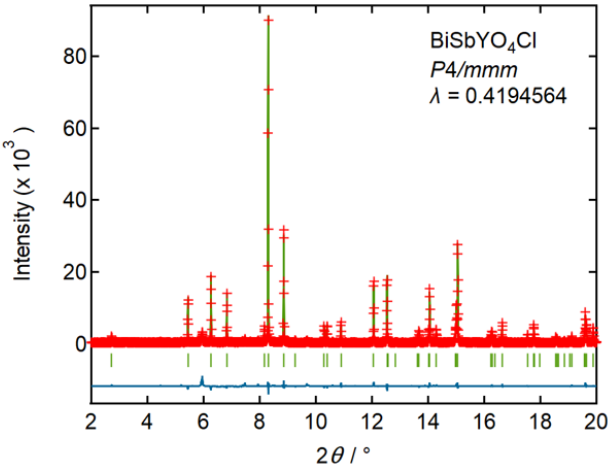
BiSbYO4Cl
P4/mmm
λ = 0.4194564
Intensity (x 10^3)
2θ / °

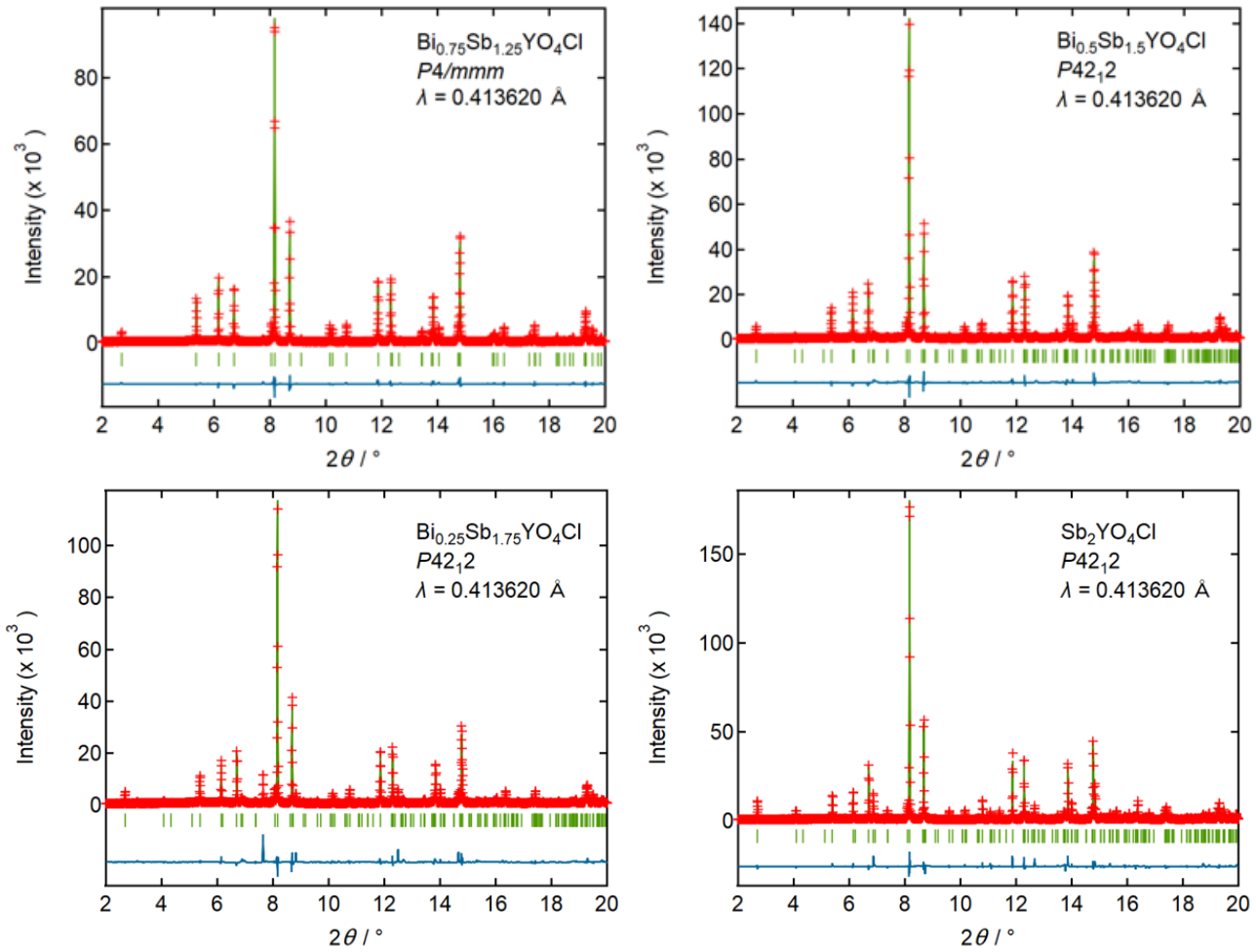

Figure S4. Rietveld refinement of SPXRD data for x = 0–2. For $0 \leq x \leq 1.25$, the refinement was performed using the Bi_2YO_4Cl (*P4/mmm*) model, while for $1.5 \leq x \leq 2$ the Sb_2YO_4Cl ($P42_12$) model was utilized. The red markers, the green solid line, and the blue solid line represent observed, calculated, and difference intensities, respectively. The green ticks indicate the calculated Bragg reflections. Refined parameters are listed in Table S2.

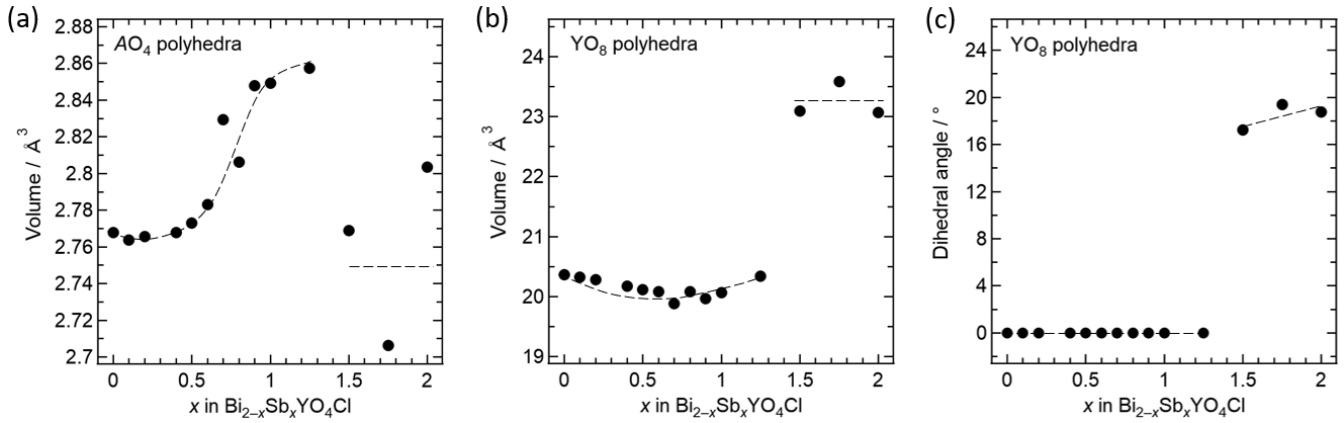

Figure S5. The volume of (a) AO_4 (A = Bi/Sb) and (b) YO_8 polyhedra. (c) The dihedral angle of YO_8 polyhedra showing its rotation. Data were obtained from Rietveld refinement of SPXRD of $Bi_{2-x}Sb_xYO_4Cl$ (x = 0–2). Broken lines are guides for the eyes.

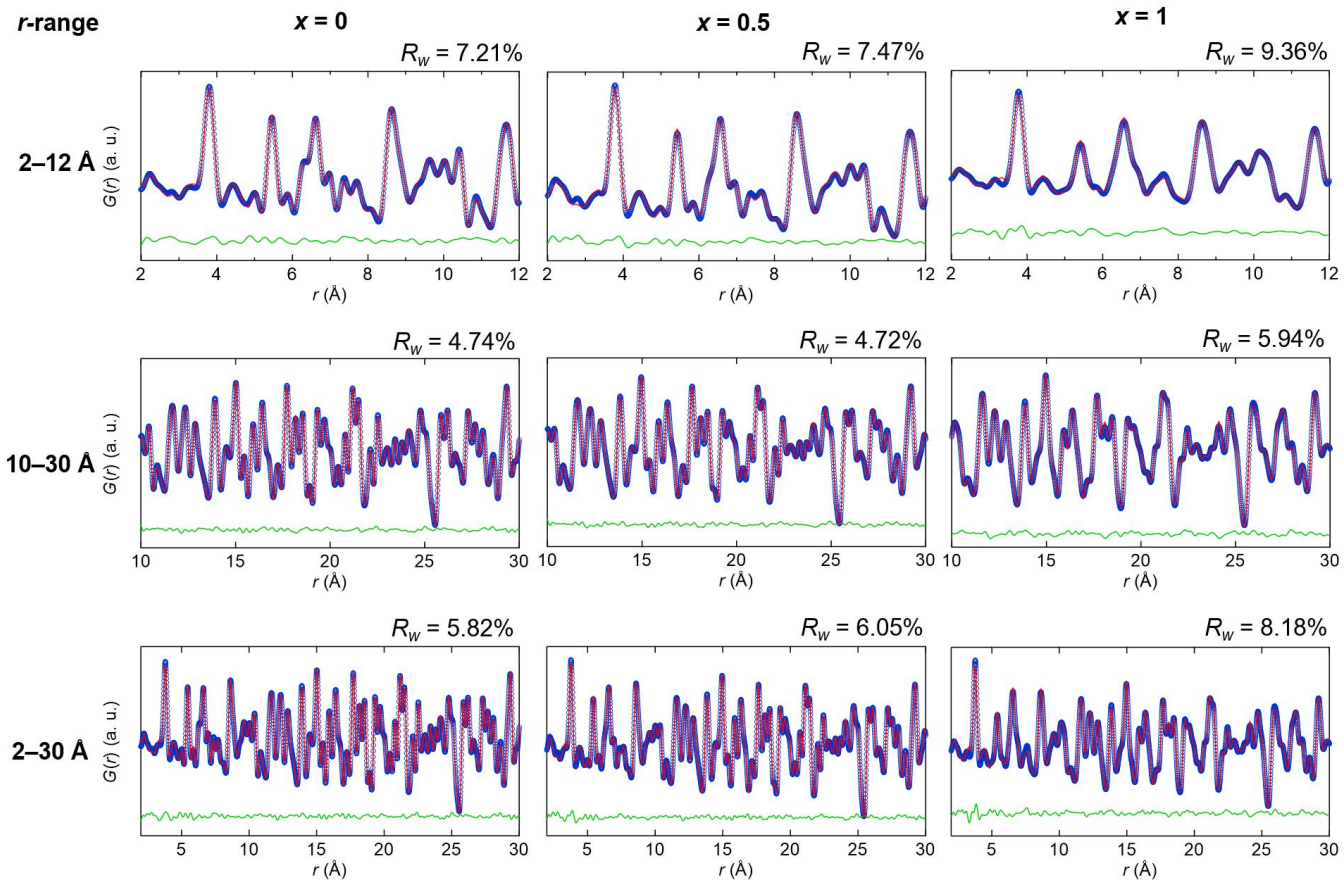

Figure S6. Profiles of X-ray PDF data of $Bi_{2-x}Sb_xYO_4Cl$ for x = 0, 0.5, and 1. Blue circles, red lines, and green lines represent experimental data, calculated data, and difference, respectively.

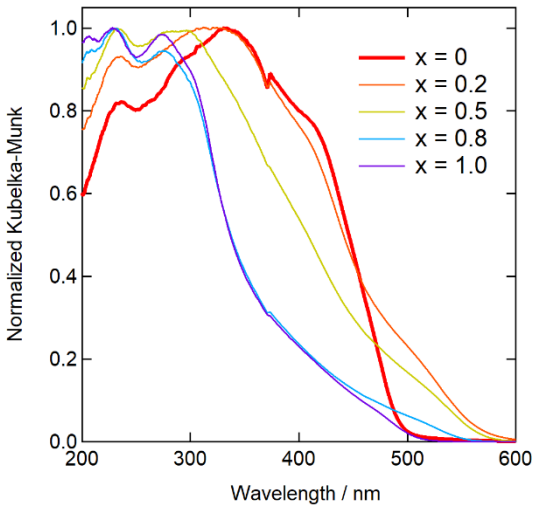

Figure S7. UV-vis diffuse reflectance spectra of $Bi_{2-x}Sb_xYO_4Cl$ (x = 0–1)

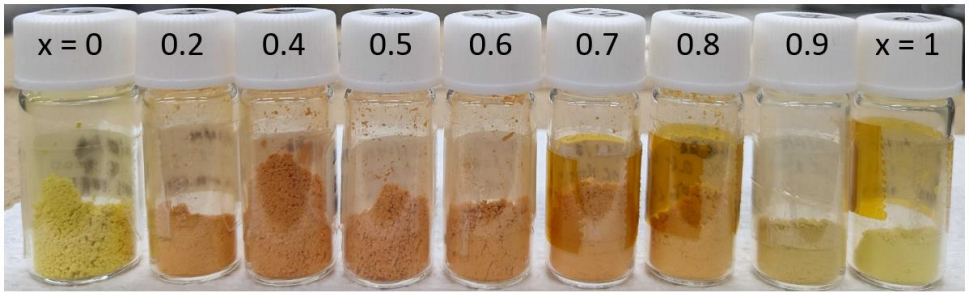

Figure S8. Colour of the as-synthesized $Bi_{2-x}Sb_xYO_4Cl$ (x = 0–1) samples

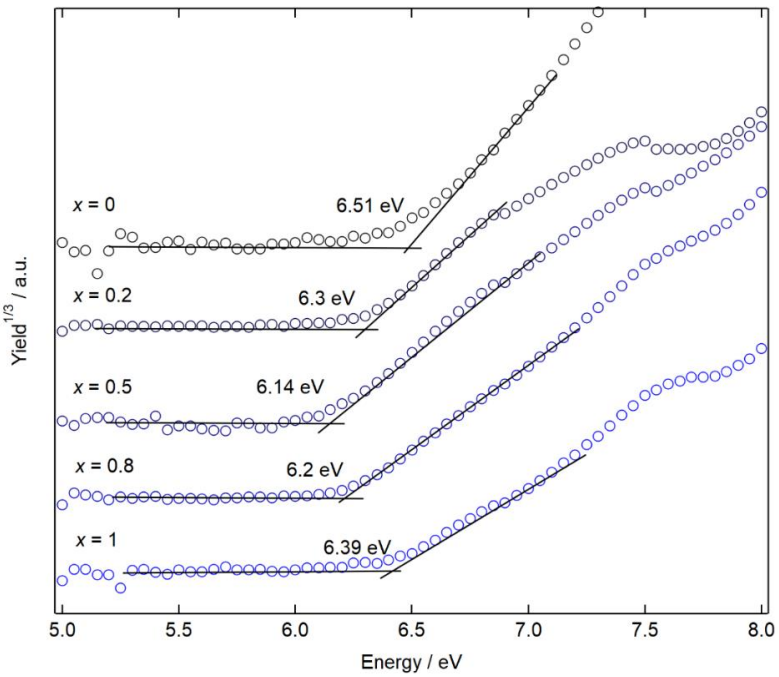

Figure S9. PYS spectra of $Bi_{2-x}Sb_xYO_4Cl$ (x = 0–1). An intersect of black lines determines the value of the ionization energy, which is shown next to each curve.

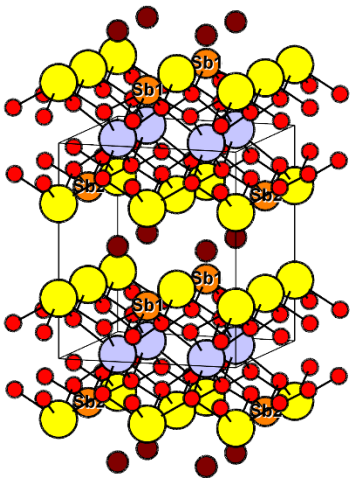

Figure S10. Supercell of $Bi_{1.5}Sb_{0.5}YO_4Cl$ used for DFT calculations. Yellow, orange, light-blue, red, and brown spheres indicate Bi, Sb, Y, O, and Cl atoms, respectively. The cutoff energy was set to 1000 eV.

5. Supporting tables

Table S1. The composition of synthesized $Bi_{2-x}Sb_xYO_4Cl$ samples observed by SEM-EDX.*

x (initial)	0	0.2	0.5	0.8	1
Cl/Cl	1	1	1	1	1
Y/Cl	1.11 (0.14)	1.00 (0.14)	0.98 (0.16)	1.03 (0.15)	1.06 (0.24)
Sb/Cl	0	0.19 (0.05)	0.53 (0.09)	0.84 (0.14)	1.08 (0.21)
Bi/Cl	2.32 (0.24)	1.88 (0.23)	1.58 (0.21)	1.23 (0.19)	1.07 (0.23)
x (observed)	0	0.18 (0.04)	0.50 (0.06)	0.81 (0.07)	1.00 (0.09)

* The *x (initial)* corresponds to the nominal composition, and the *x (observed)* is obtained from SEM-EDX. The ratio relative to Cl is shown. The average value and the deviation were calculated after measuring the composition in 10 different areas. Values in brackets show the standard deviation of the average composition.

Table S2. Crystallographic data and reliability indices obtained by the Rietveld refinement of $Bi_{2-x}Sb_xYO_4Cl$ (x = 0–2)

x = 0		*GOF* (%)	R_p (%)	R_{wp} (%)	
		1.74	5.47	7.41	
Atom	Occupancy	*x*	*y*	*z*	U_{iso} (Å^2)
Bi1	1	0.5	0.5	0.71932(4)	0.00550(5)
Y1	1	0	0	0	0.00283(18)
O1	1	0.5	0	0.8454(4)	0.0052(8)
Cl1	1	0	0	0.5	0.0135(7)
x = 0.1		*GOF* (%)	R_p (%)	R_{wp} (%)	
		1.67	6.06	8.03	
Atom	Occupancy	*x*	*y*	*z*	U_{iso} (Å^2)
Bi1	0.95	0.5	0.5	0.71891(5)	0.00563(6)
Sb1	0.05	0.5	0.5	0.71891(5)	0.00563(6)
Y1	1	0	0	0	0.0032(2)
O1	1	0.5	0	0.8452(5)	0.0053(9)
Cl1	1	0	0	0.5	0.0147(8)
x = 0.2		*GOF* (%)	R_p (%)	R_{wp} (%)	
		1.15	5.93	7.70	
Atom	Occupancy	*x*	*y*	*z*	U_{iso} (Å^2)
Bi1	0.9	0.5	0.5	0.71853(6)	0.00673(8)
Sb1	0.1	0.5	0.5	0.71853(6)	0.00673(8)
Y1	1	0	0	0	0.0026(3)
O1	1	0.5	0	0.8452(6)	0.0068(12)
Cl1	1	0	0	0.5	0.0149(10)
x = 0.4		*GOF* (%)	R_p (%)	R_{wp} (%)	
		1.57	5.62	7.45	
Atom	Occupancy	*x*	*y*	*z*	U_{iso} (Å^2)
Bi1	0.8	0.5	0.5	0.71793(5)	0.00688(8)
Sb1	0.2	0.5	0.5	0.71793(5)	0.00688(8)
Y1	1	0	0	0	0.0015(2)
O1	1	0.5	0	0.8453(5)	0.0079(10)
Cl1	1	0	0	0.5	0.0146(8)
x = 0.5		*GOF* (%)	R_p (%)	R_{wp} (%)	
		2.08	5.89	8.88	
Atom	Occupancy	*x*	*y*	*z*	U_{iso} (Å^2)
Bi1	0.75	0.5	0.5	0.71753(6)	0.00660(10)
Sb1	0.25	0.5	0.5	0.71753(6)	0.00660(10)
Y1	1	0	0	0	0.0013(2)
O1	1	0.5	0	0.8452(5)	0.0090(11)
Cl1	1	0	0	0.5	0.0142(9)
x = 0.6		*GOF* (%)	R_p (%)	R_{wp} (%)	
		2.14	6.47	8.78	
Atom	Occupancy	*x*	*y*	*z*	U_{iso} (Å^2)
Bi1	0.7	0.5	0.5	0.71704(6)	0.00801(9)

Sb1	0.3	0.5	0.5	0.71704(6)	0.00801(9)
Y1	1	0	0	0	0.0010(2)
O1	1	0.5	0	0.8455(5)	0.0109(11)
Cl1	1	0	0	0.5	0.0166(9)
***x* = 0.7**		*GOF* (%)	R_p (%)		R_{wp} (%)
		2.87	8.73		11.71
Atom	Occupancy	*x*	*y*	*z*	U_{iso} (Å^2)
Bi1	0.65	0.5	0.5	0.71638(9)	0.01712(18)
Sb1	0.35	0.5	0.5	0.71638(9)	0.01712(18)
Y1	1	0	0	0	0.0046(3)
O1	1	0.5	0	0.8470(7)	0.0167(17)
Cl1	1	0	0	0.5	0.0235(14)
***x* = 0.8**		*GOF* (%)	R_p (%)		R_{wp} (%)
		1.86	5.71		7.74
Atom	Occupancy	*x*	*y*	*z*	U_{iso} (Å^2)
Bi1	0.6	0.5	0.5	0.71616(6)	0.01062(10)
Sb1	0.4	0.5	0.5	0.71616(6)	0.01062(10)
Y1	1	0	0	0	0.0013(2)
O1	1	0.5	0	0.8456(5)	0.0161(12)
Cl1	1	0	0	0.5	0.0189(9)
***x* = 0.9**		*GOF* (%)	R_p (%)		R_{wp} (%)
		1.82	5.44		7.56
Atom	Occupancy	*x*	*y*	*z*	U_{iso} (Å^2)
Bi1	0.55	0.5	0.5	0.71568(5)	0.01303(12)
Sb1	0.45	0.5	0.5	0.71568(5)	0.01303(12)
Y1	1	0	0	0	0.00300(19)
O1	1	0.5	0	0.8468(4)	0.0220(12)
Cl1	1	0	0	0.5	0.0207(8)
***x* = 1**		*GOF* (%)	R_p (%)		R_{wp} (%)
		2.37	6.02		9.80
Atom	Occupancy	*x*	*y*	*z*	U_{iso} (Å^2)
Bi1	0.5	0.5	0.5	0.71539(8)	0.0118(2)
Sb1	0.5	0.5	0.5	0.71539(8)	0.0118(2)
Y1	1	0	0	0	0.0013(3)
O1	1	0.5	0	0.8463(6)	0.0225(17)
Cl1	1	0	0	0.5	0.0189(12)
***x* = 1.25**		*GOF* (%)	R_p (%)		R_{wp} (%)
		2.03	5.310		7.020
Atom	Occupancy	*x*	*y*	*z*	U_{iso} (Å^2)
Bi1	0.375	0.5	0.5	0.71408(7)	0.02090(17)
Sb1	0.625	0.5	0.5	0.71408(7)	0.02090(17)
Y1	1	0	0	0	0.0036(2)
O1	1	0.5	0	0.8450(5)	0.0348(14)
Cl1	1	0	0	0.5	0.0219(10)
***x* = 1.5**		*GOF* (%)	R_p (%)		R_{wp} (%)
		3.22	6.79		9.34
Atom	Occupancy	*x*	*y*	*z*	U_{iso} (Å^2)
Y1	1	0	0	0	0.0132(13)
Y2	1	0	0.5	0.0044(6)	0.0016(7)
Sb1	0.75	0.2509(2)	0.23428(19)	0.28648(10)	0.0360(4)
Bi1	0.25	0.2509(2)	0.23428(19)	0.28648(10)	0.0360(4)
O1	1	0.0348	0.2422	0.1513	0.02993
O2	1	0.4677	0.248	0.1561	0.008498
Cl1	1	0	0	0.5	0.032467
Cl2	1	0	0.5	0.5023	0.014995
***x* = 1.75**		*GOF* (%)	R_p (%)		R_{wp} (%)
		4.44	8.21		13.76
Atom	Occupancy	*x*	*y*	*z*	U_{iso} (Å^2)
Y1	1	0	0	0	0.018(4)

Y2	1	0	0.5	0.0054(11)	0.009(3)
Sb1	0.875	0.2506(3)	0.2314(3)	0.28646(17)	0.0291(6)
Bi1	0.125	0.2506(3)	0.2314(3)	0.28646(17)	0.0291(6)
O1	1	0.043(2)	0.249(4)	0.1559(16)	0.025(6)
O2	1	0.4696	0.2407	0.1622	0.014878
Cl1	1	0	0	0.5	0.009(7)
Cl2	1	0	0.5	0.500(3)	0.054(14)
x = 2		*GOF* (%)	R_p (%)	R_{wp} (%)	
		4.59	8.96	13.10	
Atom	Occupancy	x	y	z	U_{iso} (Å^2)
Y1	1	0	0	0	0.0047(4)
Y2	1	0	0.5	0.0124(4)	0.0047(4)
Sb1	1	0.25045(18)	0.21278(16)	0.28591(14)	0.0189(5)
O1	1	0.0623(15)	0.248(4)	0.1361(12)	0.028(4)
O2	1	0.4744(12)	0.253(3)	0.1703(10)	0.002(3)
Cl1	1	0	0	0.5	0.003(3)
Cl2	1	0	0.5	0.4919(15)	0.035(7)

Table S3. Refined atomic displacement parameters (ADP) in Å^2 units for $Bi_{2-x}Sb_xYO_4Cl$ (x = 0, 0.5, 1) obtained from the fit of pair distribution function (PDF) in two different r ranges

Atomic site	r-range 10–30 Å			r-range 2–12 Å		
	x = 0	x = 0.5	x = 1	x = 0	x = 0.5	x = 1
Bi/Sb	0.0049	0.0080	0.0126	0.0039	0.0069	0.0111
O	0.0268	0.0265	0.0430	0.0890	0.1071	0.0004
Y	0.0090	0.0088	0.0088	0.0083	0.0101	0.0134
Cl	0.0358	0.0439	0.0825	0.0456	0.0546	0.3340

Table S4. The lattice parameters and bandgap of $Bi_{2-x}Sb_xYO_4Cl$ (x = 0, 0.5) obtained theoretically and experimentally.*

Lattice parameters	**Bi_2YO_4Cl**		**$Bi_{1.5}Sb_{0.5}YO_4Cl$**	
	a	c	a	c
Experimental / Å	3.85048	8.88379	3.83395	8.85060
Calculated / Å	3.8972	9.0941	3.8678	9.0440
Error / %	1.21	2.37	0.88	2.18
Bandgap	**Bi_2YO_4Cl**		**$Bi_{1.5}Sb_{0.5}YO_4Cl$**	
Experimental / eV	2.5		2.1	
Calculated / eV	3.1		2.6	

* The predicted lattice parameters are in reasonable agreement with the ones obtained by Rietveld refinements within the accuracy of the DFT calculations using the PBE functional. The experimental bandgaps were obtained from Tauc plots of UV-vis reflectance spectra. Calculated bandgaps are underestimated compared with experimental ones, which is a well-known and common problem of DFT calculations using the PBE functional.[11]

Table S5. The Bi–O/Sb–O distances of the outer sublayer of the triple fluorite layer in Sb_2YO_4Cl, Bi_3O_4Cl, and Bi_2LaO_4Cl, and the corresponding bond valences. The "broken" Bi–O/Sb–O bonds are shown in bold.

Compound	Atom1	Atom2	Distance / Å	Bond valence
Sb_2YO_4Cl	Sb1	O2	2.035	0.806
	Sb1	O2	2.107	0.663
	Sb1	O1	1.981	0.932
	Sb1	**O1**	**3.003**	**0.059**
Bi_3O_4Cl [Ref 7]	Bi1	O4	2.095	0.997
	Bi1	O1	2.096	0.995
	Bi2	O3	2.128	0.912
	Bi1	**O2**	**3.325**	**0.036**
Bi_2LaO_4Cl [Ref 7]	Bi1	O4	1.98	0.680
	Bi1	O1	2.14	0.442
	Bi2	O3	2.15	0.430
	Bi1	O2	2.17	0.407
	Bi2	O2	2.21	0.365
	Bi2	O3	2.28	0.302
	Bi2	O1	2.32	0.271
	Bi1	**O4**	**3.71**	**0.006**

6. References

1 M. Schmidt, M. Oppermann, H. Hennig, C. Henn, R.W. Gmelin, E. Soeger, N. Binnewies, *Zeitschrift fuer Anorg. und Allg. Chemie*, 1950, **626**, 125–135.

2 R. J. C. Locke, F. C. Goerigk, M. J. Schäfer, H. A. Höppe and T. Schleid, *RSC Adv.*, 2022, **12**, 640–647.

3 T. Yamamoto, T. Yajima, Z. Li, T. Kawakami, K. Nakano, T. Tohyama, T. Yagi, Y. Kobayashi and H. Kageyama, *Inorg. Chem.*, 2021, **60**, 2228–2233.

4 S. Jia, P. Jiramongkolchai, M. R. Suchomel, B. H. Toby, J. G. Checkelsky, N. P. Ong and R. J. Cava, *Nat. Phys.*, 2011, **7**, 207–210.

5 K. Kudo, H. Ishii, M. Takasuga, K. Iba, S. Nakano, J. Kim, A. Fujiwara and M. Nohara, *J. Phys. Soc. Japan*, 2013, **82**, 2–5.

6 D. Kato, O. Tomita, R. Nelson, M. A. Kirsanova, R. Dronskowski, H. Suzuki, C. Zhong, C. Tassel, K. Ishida, Y. Matsuzaki, C. M. Brown, K. Fujita, K. Fujii, M. Yashima, Y. Kobayashi, A. Saeki, I. Oikawa, H. Takamura, R. Abe, H. Kageyama, T. E. Gorelik and A. M. Abakumov, *Adv. Funct. Mater.*, 2022, **32**, 1–9.

7 A. Nakada, D. Kato, R. Nelson, H. Takahira, M. Yabuuchi, M. Higashi, H. Suzuki, M. Kirsanova, N. Kakudou, C. Tassel, T. Yamamoto, C. M. Brown, R. Dronskowski, A. Saeki, A. Abakumov, H. Kageyama and R. Abe, *J. Am. Chem. Soc.*, 2021, **143**, 2491–2499.

8 Y. Yang, T. Zhu, Y. Matsumoto and H. Kageyama, *Inorg. Chem.*, 2022, **61**, 7026–7031.

9 P. Juhás, T. Davis, C. L. Farrow and S. J. L. Billinge, *J. Appl. Crystallogr.*, 2013, **46**, 560–566.

10 C. L. Farrow, P. Juhas, J. W. Liu, D. Bryndin, E. S. Boin, J. Bloch, T. Proffen and S. J. L. Billinge, *J. Phys. Condens. Matter*, DOI:10.1088/0953-8984/19/33/335219.

11 J. P. Perdew, *Int. J. Quantum Chem.*, 1985, **28**, 497–523.